Textural Entrapment of Core-Forming Melts

William G. Minarik,* Frederick J. Ryerson, E. Bruce Watson

Small volume fractions of metal-rich, iron-nickel-sulfur-oxygen melt do not form an interconnected network in polycrystalline olivine at pressures up to 11 gigapascals. These results suggest that iron-rich melts could not have migrated downward along olivine grain edges to form Earth's core. Core separation at pressures below 11 gigapascals within planetary bodies must have been facilitated by large degrees of partial melting, resulting in either separation of immiscible silicate and metal-sulfide melts or extraction of the silicate melt to concentrate the metallic remainder.

Earth and other terrestrial planets, moons, and smaller bodies have metallic cores consisting primarily of Fe and Ni, yet the process by which these cores separated from the silicate mantles is uncertain. Did Earth's core grow by separation of immiscible metal and silicate melts in a planet-scale magma ocean that formed after a large accretionary impact, or did metal-sulfide melt percolate down through an assemblage of silicate minerals? Recent contributions (*1*) have focused on the chemical implications of core formation, but an understanding of the process is required to develop better models of the composition and early thermal history of Earth's core and mantle. Core separation by means of liquid immiscibility would preserve elemental partitioning imposed at far different thermodynamic conditions than a grain-edge metallic melt percolating toward Earth's center in contact with solid silicate minerals.

Core separation accomplished by porous flow of Fe-Ni-S-O melt through a solid matrix has been viewed as unlikely because the high interfacial energies of metallic melts in contact with silicate minerals observed at low pressures do not allow the melt to wet silicate grains, precluding formation of an interconnected melt at low melt fraction (*2*). The melt-solid interfacial energy of the system can be minimized if the melt contact area is reduced; this process results in melt pockets isolated at grain corners, leading to zero permeability. The relative interfacial energies of the melt-grain edge contact can be parameterized by the dihedral angle θ, which is defined by

$$\gamma_{S\text{-}S} = 2\gamma_{S\text{-}L}\cos(\theta/2)$$

where $\gamma_{S\text{-}S}$ and $\gamma_{S\text{-}L}$ are, respectively, the solid-solid and the solid-liquid interfacial energies; $\theta > 60°$ represents nonwetting melts, and $\theta < 60°$ represents wetting melts. Recent experiments (*3*) have suggested that at higher pressures, increased solubility of O in the metal-sulfide melt may reduce the interfacial energy of the melt against silicate minerals and allow the metal-sulfide melt to wet grain edges and interconnect. To address this suggestion, we performed experiments at pressures up to 11 GPa to determine the microstructural distribution of metallic melts in an olivine matrix.

Our samples combined a sulfide-oxide mixture with olivine (grain size <38 μm) separated from a lherzolite xenolith (San Carlos, New Mexico) to simulate the upper protomantle of Earth. The initial sulfide composition was the interpolated eutectic in the Fe-Ni-S system at 10 GPa (*3*), $Fe_{59.4}Ni_{9.0}S_{31.6}$ (in atomic percent). The sulfide-oxide mixture was produced from natural pyrite and reagent-grade Fe and Ni powders to which an oxide component (powdered Fe_2O_3 and NiO) was added to ensure O saturation of the sulfide melt and the presence of a solid oxide phase. Additional Fe metal was added to the eutectic sulfide mixture to replace Fe lost from the melt to produce Fe-enriched olivine and (Mg,Fe) oxide (*4*).

We conducted experiments at or below 4 GPa in a piston-cylinder device (*5*). In order to reduce the porosity in the sample and capsule before the sulfide melted, we maintained runs at the final pressure and 700°C for 30 min before increasing the temperature to 1500°C (*6*). The sulfide-olivine mix was contained within MgO or graphite capsules (both with and without a Pt outer capsule) and separated from the graphite furnace by a ceramic sleeve. No difference was seen between graphite-encapsulated runs with and without a Pt outer capsule, suggesting that the graphite capsules are sealed with respect to S-rich vapor (*7*). We ran two graphite-encapsulated experiments (at 1500°C) at 9 GPa and 11 GPa and in the split-cone multianvil press, using 8-mm truncated-edge-length carbide anvils (*8*, *9*).

Melt composition depends on the bulk composition of the system, the oxygen fugacity (f_{O_2}), and the pressure-dependent partitioning of Fe, Ni, and Mg between melt, olivine, and oxide. We did not control f_{O_2} in these experiments, but it is constrained to be greater than that needed to stabilize (Mg,Fe)O and olivine and less than the maximum stability limit of the graphite or diamond capsule. No carbonate or orthopyroxene was observed, which further constrained f_{O_2} to be below the olivine + diamond + O_2 = pyroxene + carbonate reaction [or EMOD (*10*)]. The O content of the sulfide melt was expected to increase with increasing pressure and temperature (*3*); however, we found that the O contents of the melts at 3 to 4 and 9 to 11 GPa are roughly similar but poorly determined, as the O content has been modified by the precipitation of oxide during quenching from high temperature (Table 1).

We measured θ for each experiment (all samples contained quenched sulfide melt dispersed along the grain corners of the olivine and oxide matrix). The sulfide melt quenched to an intergrowth of dendritic metal and Fe-Ni sulfide (Fig. 1). No gravitational segregation of sulfide was observed in our samples that contained up to 9% (by volume) metal-sulfide melt. We ran three experiments with the same melt composition for 4, 24, and 96 hours at 3.9 GPa to

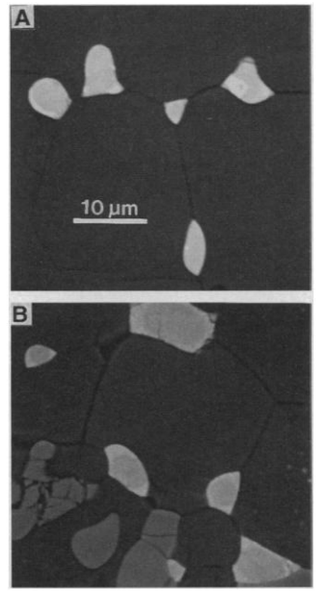

Fig. 1. (**A** and **B**) Backscattered electron photos of the 9-GPa (MA-18) experiment showing metal-sulfide pockets (light gray) at olivine grain corners (dark gray), now composed of an intergrowth of metal alloy, sulfide, and oxide formed on quench. Oxide has separated on quench as a thin rim on the sulfide pockets and is also present as a stable phase (medium gray). The grain edges are sulfide-free and sulfide is included within the olivine grains, consistent with the large apparent values of θ at the corner of the melt pockets.

W. G. Minarik and F. J. Ryerson, Institute for Geophysics and Planetary Physics, L-202, Lawrence Livermore National Laboratory, Post Office Box 808, Livermore, CA 94551, USA.
E. B. Watson, Department of Earth and Environmental Sciences, Rensselaer Polytechnic Institute, Troy, NY 12180, USA.
*To whom correspondence should be addressed.

Table 1. Experimental conditions and average compositions of the quenched sulfide melt recalculated to atomic percent. All experiments were performed at 1500°C. Because the melts quench to a heterogeneous assemblage of phases, there is considerable variation among analyses, even with broad-beam analysis. The standard deviation about the average is given in parentheses. All totals lay within the range of 97.5 to 100.5% (by weight). We analyzed samples for Fe, Ni, S, Si, Mg, and O using metal, sulfide, and oxide standards on a JEOL 733 electron microprobe at 15 keV. We measured the K_α oxygen line directly with an Ovonyx Ni/C multilayer crystal, using Al_2O_3 as a standard. We analyzed sulfides at a current of 25 nA, using a rastered defocused beam; to measure oxides and olivine, we used a current of 50 nA and a focused beam. We corrected x-ray raw intensity ratios for matrix effects using a phi-rho-Z program supplied by Tracor-Northern.

Experiment number	Pressure (GPa)	Duration (hours)	Capsule material	Number of analyses	Composition (atomic %)			
					Fe	Ni	S	O
PC-112	4.0	24	MgO	20	44.99 (0.96)	11.95 (1.42)	38.67 (0.86)	4.39 (0.68)
PC-113	4.0	24	MgO + C	28	47.90 (0.85)	9.50 (1.12)	39.40 (0.78)	3.20 (0.65)
PC-117	3.9	13	Graphite	24	37.80 (0.91)	9.90 (0.98)	44.50 (0.87)	7.80 (0.87)
PC-119	4.0	21	Graphite	17	39.51 (0.63)	10.99 (0.83)	41.36 (0.84)	8.13 (1.15)
PC-148	3.5	24	Graphite	23	36.40 (0.79)	19.10 (0.87)	39.10 (0.74)	5.40 (0.77)
PC-190	3.5	96	Graphite	21	41.08 (0.84)	13.27 (1.23)	43.82 (0.83)	1.84 (0.45)
PC-191	3.5	4	Graphite	25	42.10 (0.93)	14.21 (1.03)	40.18 (0.87)	3.51 (0.62)
MA-18	9	4	Diamond	20	37.23 (0.77)	15.73 (1.41)	43.80 (0.88)	3.24 (0.68)
MA-26	11	22	Diamond	22	40.42 (0.72)	10.20 (0.86)	45.30 (0.34)	4.07 (0.59)

investigate the effect of run duration on microstructure (experiments PC-191, -148, and -190). Small olivine grains and small sulfide pockets coalesced in the longer runs as the olivine coarsened and the overall interfacial energy of the system was reduced, but no significant difference in θ was observed (Table 2).

The solid-melt interfacial energy $\gamma_{S\text{-}L}$ is a function of composition and is expected to decrease with increasing structural similarity between the melt and solid, resulting in a decrease in θ for a constant solid-solid interfacial energy $\gamma_{S\text{-}S}$. The values of θ determined at 9 and 11 GPa are slightly larger but similar to those of the runs at 3 to 4 GPa for similar contents of light elements (Figs. 2 and 3). The high values of θ of the runs at 9 to 11 GPa indicate that changes in melt composition or structure up to these pressures are not sufficient to alter the high olivine-sulfide melt interfacial energy and allow an interconnected melt to exist at low melt fraction.

The measured values of θ decreased as the S or S + O content increased in the melts. The results of an experiment (PC-117) with a high-S melt [(S + O) > (Fe + Ni)] at a pressure of 4 GPa suggested that this melt does partially interconnect, with θ near the critical 60° angle. This trend is consistent with the low surface energy in S-rich Fe-Ni slag systems at low pressure (*11*) and with the observation from experiments with an LL3 chondrite in which sulfide-rich melts were mobile and seemed to produce an interconnected grain-edge liquid (*12*). The eutectic composition becomes more Fe-rich with increasing pressure (*3*), making the PC-117 melt composition more S-rich than the eutectic composition at all pressures, and it would not be the first melt formed during sulfide melting.

Experiments performed by Shannon and Agee (*13*) show that sulfide melts produced by melting an ordinary chondrite do not wet silicate minerals up to pressures of 9 GPa, consistent with our results. Herpfer and Larimer (*14*) reported that at 1300°C

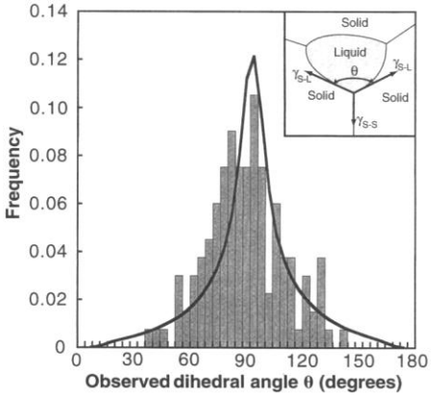

Fig. 2. Apparent values of θ determined from 133 sulfide-olivine contacts (bars) for sulfide-olivine contacts in the 9-GPa experiment along with the expected distribution (line) for a single θ centered at the median θ value of 93°. The solid-solid-melt boundaries of a sectioned experiment will show a distribution of apparent θ due to the plane of the section crossing the grain edge at a random orientation. The median value of θ of this distribution is an approximation of the true θ in systems with a single characteristic wetting angle (*27*). We have broadened the theoretical distribution assuming a measurement error with a standard deviation of 2°. In general, silicates and oxides have anisotropic surface energies (surface energy varies with crystallographic orientation) that will broaden the observed θ distribution (*28*). The inset defines θ and its relation to the interfacial energies.

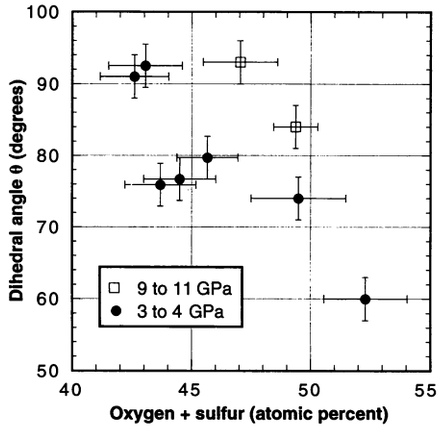

Fig. 3. Median measured values of θ as a function of the content of light elements in the melt. Only when S + O exceeds ~50 mol% do the melts begin to form an interconnected network along grain edges. Values of θ remain large at pressures up to 11 GPa and show no systematic variation with O content. Error bars show 1 SD about the mean of the electron microprobe analyses from Table 2 and show an uncertainty in θ of ± 3°.

Experiments performed by Shannon and Agee (*13*) show that sulfide melts produced by melting an ordinary chondrite do not wet silicate minerals up to pressures of 9 GPa, consistent with our results. Herpfer and Larimer (*14*) reported that at 1300°C

Table 2. Number of angles measured and the median measured value of θ for each experiment. We digitized each interface of a melt-olivine contact angle with 4 to 8 points at ×1560 power using a digitizing tablet and a through-the-scope light-emitting diode display designed for fission-track measurements. A polynomial was fitted to these digitized points, and the tangents to the curves at the intersection point (the vertex) were used to define the measured angle. All measurable angles within an area of the section were digitized to avoid adding selection bias to the resulting distribution. The standard deviation about the average is given in parentheses.

Experiment number	Number of angles measured	Median θ (degrees)	O + S (atomic %)
PC-112	134	92.5	43.06 (1.54)
PC-113	176	91	42.60 (1.43)
PC-117	227	60	52.30 (1.74)
PC-119	110	74	49.49 (1.99)
PC-148	139	76.7	44.50 (1.51)
PC-190	153	79.7	45.66 (1.28)
PC-191	110	75.9	43.69 (1.49)
MA-18	133	93	47.04 (1.56)
MA-26	167	84	49.37 (0.93)

and 1 GPa the Fe-FeS eutectic composition in contact with olivine has $\theta = 55°$ and would form an interconnected melt. We see no evidence of dihedral angles in this range between the eutectic and the (Fe,Ni)S composition at 1500°C and 4 to 11 GPa. The melts in the experiments of Herpfer and Larimer lost Fe to the olivine, resulting in an actual melt composition more S-rich than the Fe-FeS eutectic. Their low measured values of θ are consistent with ours if their melts have Fe/S < 1.

These experiments demonstrate that textural equilibration of metal-sulfide melts and olivine does not result in a microstructure that would allow separation by porous flow at low melt fraction. At sufficiently high melt fraction, melts that do not wet grain edges (those with $\theta > 60°$) eventually become interconnected. The melt fraction at which connectivity occurs can be estimated theoretically for systems with homogeneously distributed melt by (*15*):

$$f_c \approx 0.009(\theta - 60)^{1/2}$$

where f_c is the melt fraction at the onset of connectivity. Melts with $\theta = 90°$ to 100° should begin to connect at about 5% (by volume). However, the melt does not remain homogeneously distributed at these high values of θ. Melt-free grain edges are still energetically favored, causing the melt blebs to coalesce into larger blebs surrounded by dry grain edges. Permeability therefore remains low at melt fractions greater than the theoretical value for interconnectivity (*2*). Textures observed in our runs and those reported for other experiments in which sulfide melts were used (*6, 16*) show larger blebs of sulfide melt surrounded by dry grain edges. These experimental textures and meteorite studies suggest that the actual melt fraction for the formation of an interconnected metallic melt may be as high as 40% (by volume) (*2, 17*). Jurewicz and Jones (*18*) reported that subsolidus experiments with Fe metal in an olivine matrix became electrically conductive and hence interconnected near 20% (by volume) metal.

Our results imply that metal-rich melts cannot separate from olivine by porous flow at low melt fraction in bodies less than 2500 km in diameter (corresponding to center pressures of 11 GPa) (*19*). Iron and stony-iron meteorites are inferred to represent relicts of cores in the parent planetesimals. Textural and chemical evidence implies that metal-silicate separation in these bodies required high temperatures and extensive melting of the silicate portions, whereas meteorites that display incomplete metal separation are characterized by small extents of silicate melting (*17*). The pressure at the center of Earth's moon is 4.6 GPa, well within the olivine stability field, and the moon is likely depleted in S as it is in other volatile elements. Hence, separation of an S-poor metal core in the moon [estimated to be 0 to 2% of the lunar mass (*20*)] would require extensive melting of the silicate mantle.

The maximum pressure used in our study corresponds to a depth of 350 km in the present Earth's mantle: the silicate solidus here is near 1800°C (*21*), and downward percolation of metallic melts is precluded to this depth. Nonwetting metal-sulfide melts provide a physical basis for models of core formation that invoke incomplete separation of metallic core from silicate mantle. Small amounts of metallic melt could be left behind after core separation [the "inefficient core formation model" (*22*)] entrapped as isolated melt pockets at grain corners. Late-stage accretion of metal after core formation and the last large-impact melting could also be retained in the mantle [(*23*) or the "late-stage veneer model" (*24*)]. In both cases, the metallic melt retained in the mantle would contribute siderophile elements and produce a mantle that was not in chemical equilibrium with the core. Core formation by separation of a eutectic sulfide melt instead of a metal alloy (*25*) also requires melting of the silicate matrix. The eutectic sulfide melt does not contain enough S to form an interconnected melt and hence would not separate at low melt fraction and percolate toward the core. Heterogeneous accretion models that require continued core accumulation by separation of a small amount of metal-sulfide are difficult to reconcile with these results unless accompanied by repeated extensive mantle melting (*26*).

Earth's core may have been assembled from the cores of accreted planetesimals whose compositions reflect high-temperature, low-pressure equilibrium and were then modified over time by interaction with mantle silicates at core-mantle boundary pressures. If the magma ocean did not encompass the entire volume of the body, a pond of metallic melt at the bottom of an impact-heated zone would only be able to join the core if it was massive enough to sink diapirically through the solid silicate below.

Our results do not preclude the existence of interconnected metal-sulfide melts at higher pressures. The quantity θ is sensitive to small changes in the melt-solid interfacial energy; a reduction in θ from 70° to 60° requires only a 5% decrease in the relative melt-olivine interfacial energy. Modification of melt composition of structure at pressures >11 GPa may decrease the θ of a likely core-forming composition enough to allow it to interconnect. Similarly, a change in solid assemblage from olivine-dominated to spinel-, majorite garnet–, or $(Mg,Fe)SiO_3$ perovskite–dominated assemblages could also reduce θ.

REFERENCES AND NOTES

1. V. R. Murthy, *Science* **253**, 303 (1991); D. Walker, L. Norby, J. H. Jones, *ibid.* **262**, 1858 (1993); V. J. Hillgren, M. J. Drake, D. C. Rubie, *ibid.* **264**, 1442 (1994); H. E. Newsom and K. W. W. Sims, *ibid.* **252**, 926 (1991).
2. D. J. Stevenson, in *Origin of the Earth*, H. E. Newsom and J. H. Jones, Eds. (Oxford Univ. Press, New York, 1990), pp. 231–250.
3. S. Urakawa, M. Kato, M. Kumazawa, in *High Pressure Research in Mineral Physics*, M. H. Manghnani and Y. Syono, Eds. (TerraPub–American Geophysical Union, Tokyo–Washington, DC, 1987), pp. 95–111.
4. All materials were ground to pass through a 400-mesh sieve and stored at 110°C to promote dryness. Both NaCl-Pyrex and $BaCO_3$ pressure media surrounding a graphite furnace were used in the piston-cylinder runs; temperature was controlled by means of a W3%Re–W25%Re thermocouple not adjusted for the effect of pressure.
5. F. R. Boyd and J. L. England, *J. Geophys. Res.* **65**, 741 (1960).
6. D. Walker and C. B. Agee, *Meteoritics* **23**, 81 (1988).
7. C. L. Peach and E. A. Mathey, *Geochim. Cosmochim. Acta* **57**, 3013 (1993).
8. We calibrated the pressure of multianvil runs against hydraulic pressure using the room-temperature Bi and ZnTe transitions and the 1200°C coesite-stishovite transition [T. Yagi and S.-I. Akimoto, *Tectonophysics* **35**, 259 (1976)]. We monitored and controlled the run temperature using a W5%Re–W26%Re thermocouple. The axial thermocouple was within 0.5 mm of the capsule end, and we estimate that the temperature difference between thermocouple and capsule center was 50° to 75°C. The capsule was separated from the Rh furnace by magnesia spacers, and the capsule-furnace assembly was encased in a zirconia sleeve and surrounded by a cast Aramco 584 MgO octahedron with integral gaskets [D. Walker, *Am. Mineral.* **76**, 1092 (1991)]. The run was pressurized over several hours, brought to run temperature, and then quenched by a reduction in furnace power; pressure was then slowly released overnight.
9. The recovered capsules were mounted in epoxy, sectioned, and polished for electron microprobe analysis. The graphite capsules of the multianvil runs had for the most part converted to diamond and therefore initial sectioning was done on a diamond surface grinder, followed by diamond lapping. In the final polishing we used a colloidal silica polisher, which minimized plucking, and polished the silicate and sulfide around the protruding diamond of the capsule. We measured the distributions of apparent θ by following the procedure of E. B. Watson and J. M. Brenan [*Earth Planet. Sci. Lett.* **85**, 497 (1987)].
10. D. H. Eggler and D. R. Baker, in (*3*), pp. 237–250.
11. S. W. Ip and J. M. Toguri, *Metall. Trans. B* **24**, 657 (1993).
12. H. Y. McSween Jr., L. A. Taylor, M. E. Lipschutz, *Proc. Lunar Planet. Sci. Conf.* **9**, 1437 (1978).
13. M. C. Shannon and C. B. Agee, *Eos* (suppl.) **76**, F698 (1995).
14. M. A. Herpfer and J. W. Larimer, *Meteoritics* **28**, 362 (1993); M. A. Herpfer, thesis, Arizona State University (1992).
15. N. von Bargen and H. S. Waff, *J. Geophys. Res.* **91**, 9261 (1986).
16. E. Takahashi, *Proceedings of the 8th Symposium on Antarctic Meteorites* (National Institute of Polar Research, Tokyo, Japan, 1983), vol. 30, p. 168.
17. G. J. Taylor, *J. Geophys. Res.* **97**, 14717 (1992).
18. S. R. Jurewicz and J. H. Jones, *Proc. Lunar Planet. Sci. Conf.* **26**, 709 (1995).
19. K. Keil and L. Wilson, *Earth Planet. Sci. Lett.* **117**, 111 (1993).
20. J. O. Dickey *et al.*, *Science* **265**, 482 (1994).
21. C. Herzberg, T. Gasparik, H. Sawamoto, *J. Geophys. Res.* **95**, 15779 (1990).
22. J. H. Jones and M. J. Drake, *Nature* **322**, 221 (1986).
23. W. B. Tonks and H. J. Melosh, *J. Geophys. Res.* **98**, 5319 (1993).
24. H. Wänke and G. Dreibus, *Philos. Trans. R. Soc. London Ser. A* **325**, 545 (1988).

25. R. Brett, *Geochim. Cosmochim. Acta* **48**, 1183 (1984).
26. I. Y. Azbel, I. N. Tolstikhin, J. D. Kramers, G. Pechernikova, A. V. Vityazev, *ibid.* **57**, 2889 (1993).
27. S. R. Jurewicz and A. J. G. Jurewicz, *J. Geophys. Res.* **91**, 9277 (1986).
28. W. F. Brace and J. B. Walsh, *Am. Mineral.* **47**, 1111 (1962); H. S. Waff and U. H. Faul, *J. Geophys. Res.* **97**, 9003 (1992).
29. We thank M. Hirschmann for discussions that motivated the initial experiments, and G. Gwanmesia, B. Li, and R. Lieberman, who helped with preliminary multianvil work. Reviews by J. Brenan, D. Farber, and N. Marchildon improved the manuscript. Supported by the Lawrence Livermore National Laboratory Institute of Geophysics and Planetary Physics (F.J.R.) under the auspices of Department of Energy contract W-7405-Eng-48. Additional support was provided by National Science Foundation grants EAR-8717341 and EAR-9105055 to E.B.W.

7 December 1995; accepted 12 March 1996

Role of Type I Myosins in Receptor-Mediated Endocytosis in Yeast

M. Isabel Geli and Howard Riezman*

Type I myosins are thought to drive actin-dependent membrane motility, but the direct demonstration in vivo of their involvement in specific cellular processes has been difficult. Deletion of the genes *MYO3* and *MYO5*, which encode the yeast type I myosins, almost abolished growth. A double-deleted mutant complemented with a *MYO5* temperature-sensitive allele (*myo5-1*) showed a strong defect in the internalization step of receptor-mediated endocytosis, whereas the secretory pathway remained apparently unaffected. Thus, myosin I activity is required for a budding event in endocytosis but not for several other aspects of membrane traffic.

Type I myosins constitute a large family of ubiquitous actin- and adenosine triphosphate (ATP)–dependent molecular motors with a distinct COOH-terminal tail domain. Instead of the coiled-coil region that allows dimerization of conventional myosins, type I myosins possess a short positively charged tail that in many cases binds acidic phospholipids (*1*). Their biochemical characteristics and subcellular localization to intracellular membranes suggest an involvement in actin-dependent membrane motility processes such as organelle movement, vesicle trafficking, phagocytosis, pinocytosis, membrane ruffling, or lamellipodia formation (*2*). However, direct demonstration of their requirement in vivo for these functions has been difficult because of their functional redundancy and the lack of established quantitative functional assays (*1*).

Only one type I myosin has been described in the yeast *Saccharomyces cerevisiae*: Myo3p. Deletion of the *MYO3* gene does not lead to any phenotypic change, which suggests functional redundancy (*3*). We have used a polymerase chain reaction (PCR) screening approach (*4*) to isolate a second gene, *MYO5*, that encodes a type I myosin with 87% amino acid sequence identity to Myo3p (Fig. 1A). The head and tail domains are separated by three IQ (isoleucine-glutamine) motifs, which would be predicted to bind calmodulin, a key regulator of myosin I activity (*2*). A second level of regulation is specifically provided in type I myosins by a phosphorylation site placed between the ATP and the actin binding sites [S357 (Ser^{357})] (*5*). Phosphorylation in vitro of the ameboid type I myosins causes a 20-fold activation of the adenosine triphosphatase activity (*5*). The tail of Myo5p contains two distinct features that are shared with other yeast and ameboid type I myosins: a proline-rich region that may constitute a second ATP-independent actin binding site, and an SH3 (Src homology 3) domain proposed to mediate protein-protein interaction (*2*). Recently, two SH3-containing type I myosins have been isolated from mammalian cells (*6*). The yeast Myo5p and Myo3p show maximal homology to *Acanthamoeba* myosin IB (AMIB) and *Dictyostelium* myosin IB (*7*). Both myosins localize to the plasma membrane. The phosphorylated form of AMIB concentrates to actively motile regions of the plasma membrane (*7*). Double-deletion mutants in *Dictyostelium* type I myosins (*myoA*/*myoB*$^-$ or *myoC*/*myoB*$^-$) show conditional defects in fluid-phase pinocytosis (*7*). Deletion of *MYO5*, as with deletion of *MYO3* (*3*), did not lead to any observable alterations in growth properties (*8*). However, combination of both deletions in the same haploid resulted in a severe growth defect (*9*).

One of the main processes that requires plasma membrane deformation in nonmitotic yeast is the internalization step of endocytosis. Actin and calmodulin, two key proteins associated with myosin function, are required in this process (*10*). Thus, it is possible that a type I myosin could play a role in the uptake step of receptor-mediated endocytosis.

Endocytic internalization can be monitored by measurement of the percentage of ^{35}S-labeled α-factor bound to its receptor (Ste2p), which becomes resistant to an acid wash (pH 1) over time (*11*). We used this assay to measure the efficiency of receptor-mediated internalization in *myo3*Δ and *myo5*Δ mutant strains (*9*) (Fig. 1, B and C). The *myo3*Δ strain showed wild-type (WT) internalization kinetics. In contrast, we detected a strong internalization defect in the

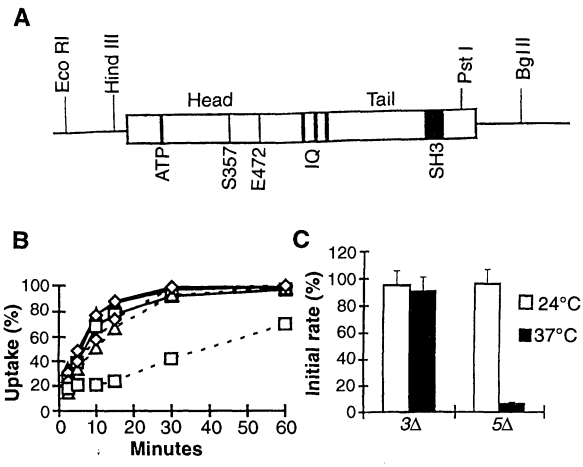

Fig. 1. *myo5*Δ but not *myo3*Δ is defective for α-factor internalization. (**A**) Structure of *MYO5* (GenBank/EMBL/DDBJ accession number SC9718; open reading frame 15772 to 19429). IQ, IQ motifs; ATP, ATP binding site; S357, putative phosphorylation site; SH3, SH3 domain. (**B**) RH3376 (WT, triangles), RH3377 (*myo3*Δ, diamonds), and RH3378 (*myo5*Δ, squares) (*9*) were assayed at 24°C (solid lines) or 37°C (dashed lines) as described (*11*). Cells were grown to logarithmic phase in synthetic dextrose yeast extract (SDYE) at 24°C. Biosynthetically labeled ^{35}S–α-factor was bound for 45 min on ice in yeast extract, peptone, uracil, adenine, and dextrose (YPUAD) medium. Cells were centrifuged and resuspended in YPUAD medium at 24°C or 37°C. Samples were taken at the indicated time points into pH 1 and pH 6 buffer to monitor internalized versus total cell-associated radioactivity. The results are expressed as the percentage of total counts internalized. The values correspond to the average of at least two independent experiments, with standard deviations smaller than 10% (20% at the initial time point). (**C**) The initial uptake rates (internalized counts per minute) were calculated for each experiment in the linear range. The average value of each mutant strain was divided by the corresponding WT values at the appropriate temperature and expressed as a percentage.

Department of Biochemistry, Biozentrum, University of Basel, Klingelbergstrasse 70, Basel, CH-4056, Switzerland.

*To whom correspondence should be addressed.